The infrared spectrum of cyclic-N_3: Theoretical prediction

Dmitri Babikov[1,a)] and Brian K. Kendrick[2]
[1]*Department of Chemistry, Marquette University, P.O. Box 1881, Milwaukee, Wisconsin 53201, USA*
[2]*Theoretical Division (T-1, MS B268) Los Alamos National Laboratory, Los Alamos, New Mexico 87545, USA*

(Received 22 July 2010; accepted 11 September 2010; published online 3 November 2010)

We have carried out the first calculations of the infrared absorption spectrum of cyclic-N_3. Accurate vibrational energies and wave functions computed with incorporation of the geometric phase effect (via gauge theory) and using an *ab initio* potential energy surface were employed in this work. A sophisticated fully dimensional dipole moment function was constructed using accurate *ab initio* calculations and a three-dimensional-spline interpolation. Transformation of the dipole moment vector function from the reference frame associated with instantaneous principal axes of inertia to the laboratory-fixed reference frame was carried out using hyperspherical coordinates. We found that the permanent dipole moment of cyclic-N_3 in the ground vibrational state is relatively small (170 mD). The excited vibrational states show permanent dipole moments in the 10–25 mD range. The most intense part of the infrared absorption spectrum is observed in the deep infrared part of spectrum, 75–275 cm^{-1}, where five lines exhibit absolute absorption intensities in the range between 0.5 and 1.2 km/mol. These transitions correspond to excitation of the pseudorotational progression of states. Several unique spectroscopic features discussed in the paper should help to identify cyclic-N_3 in the laboratory. © *2010 American Institute of Physics*. [doi:10.1063/1.3495952]

I. INTRODUCTION

The first experimental evidence of cyclic-N_3 was found in 2003 by Wodtke and co-workers[1,2] in their studies of ClN_3 photolysis at 235 nm

$$ClN_3(X^1A'') + h\nu \rightarrow Cl + N_3(\text{linear azide}),$$

$$\rightarrow Cl + N_3(\text{cyclic azide}),$$

$$\rightarrow NCl + N_2,$$

where the radical channels are dominant and account for ~95% of the fragmentation events. Using the velocity map imaging technique they obtained the kinetic energy distribution of the photofragments, which also provided the low-resolution spectrum of the internal energy in N_3 products. Their spectrum showed a very pronounced bimodal structure and demonstrated clearly that, in addition to the well known weakly bound linear-N_3, there is another energetic form of N_3 radical. This finding was in good agreement with earlier *ab initio* calculations of Bittererová *et al.*,[3] who predicted the metastable N_3 isomer ($^2B_1$) in the form of an acute isosceles triangle at energy about 1.30 eV above the linear-N_3 isomer. Further experimental evidence of cyclic-N_3 was obtained by Wodtke and co-workers[4,5] in the photofragmentation translational spectroscopy studies of ClN_3 photolysis at 248 nm and in the photoionization of N_3 products using the synchrotron vacuum uv-light source.[6,7] Cyclic-N_3 is a truly fascinating new molecule, interesting from the practical perspective, as well as from the fundamental science point of view. For recent review of experimental and theoretical work on azide photochemistry, see Refs. 8 and 9.

All low-resolution experimental data[1,2,4–7] available for cyclic-N_3 are consistent with theoretical picture of this molecule,[3,10–15] however the final proof for the existence of cyclic-N_3 is yet to be made by means of the high-resolution spectroscopy. Several possibilities are being discussed, including the photoelectron spectroscopy,[15] the matrix isolation spectroscopy, and the infrared spectroscopy. In this paper we focus on the latter and offer a theoretical prediction of the infrared absorption spectrum of cyclic-N_3.

Predicting the infrared spectrum of cyclic-N_3 appears to be a nontrivial task due to several special properties of this molecule. First of all, cyclic-N_3 is a Jahn–Teller molecule that exhibits conical intersection at the equilateral triangle configurations.[10,12] At the point of conical intersection the symmetry of the electronic wave function changes (from $^2B_1$ to $^2A_2$), which leads to the geometric phase effect. In many Jahn–Teller molecules the geometric phase effect is minor (due to high pseudorotation barriers), but in the case of cyclic-N_3 it is exceptionally large. This effect modifies the spectrum of vibrational eigenstates of cyclic-N_3 very significantly, leading to the shifts on the order of 100 cm^{-1} for the low lying vibrational states, and on the order of 600 cm^{-1} for the states close to the conical intersection.[11] Such dramatic effects are due to an almost-free pseudorotational motion enabled by the zero-point energy. In this sense the vibrational motion of cyclic-N_3 along the pseudorotational coordinate is extremely floppy, and the wave functions are extremely delocalized. They encircle the conical intersection and occupy a donutlike part of space around it.[11] It also appears that such pseudorotational motion leads to rotation of the dipole moment vector in space (even in the absence of the overall rotation of the molecule, $J=0$) which results in significant cancellation of the dipole moment averaged over

[a)]Electronic mail: dmitri.babikov@mu.edu.

the vibrational wave functions. All these effects should be treated rigorously in order to obtain correct prediction of line positions and intensities.

In Sec. II of this article we briefly review our theoretical framework and explain how we transform the dipole moment vector function from the body-fixed reference frame associated with the instantaneous principal axes of inertia of the molecule to the laboratory-fixed reference frame using the adiabatically adjusting principal-axes hyperspherical coordinates. Section III contains prediction of the infrared absorption spectrum and description of the most intense transitions. Conclusions and discussion of possible routes for experimental validation are given in Sec. IV.

II. THEORETICAL AND COMPUTATIONAL METHODS

A. Energies and wave functions of vibrational states

The energies and wave functions of vibrational states of nonrotating ($J=0$) cyclic-N_3 were computed using adiabatically adjusting principal-axes hyperspherical (APH) coordinates and the sector-adiabatic coupled-channel technique.[16] In this approach, the full dimensional Schrödinger equation for the vibrational motion is solved in two steps which can be thought of as numerical "decoupling" of different degrees of freedom. First, the hyper-radius ρ is partitioned into a large number of sectors (intervals) and the two-dimensional angular part of the Schrödinger equation (θ,φ) is solved numerically for each sector with $\rho=\rho_\xi$ fixed (as a parameter) at the center of each sector.[16] The potential coupling matrices and overlap matrices between the neighboring sectors are also computed at this step. In the second step, a set of one-dimensional coupled-channel equations is obtained for the hyper-radial coordinate ρ and is solved using a numerical propagation technique.[16] In this procedure, the coupling is recovered and the accurate full dimensional solutions of the Schrödinger equation are obtained using the exact Hamiltonian and including all couplings. Our code employs an efficient hybrid FBR/DVR (Ref. 17) algorithm to solve the angular (θ,φ) part of the problem and uses Numerov propagator[18] for solving the coupled-channel equations in ρ. Accurate *ab initio* potential energy surface is employed.[10] The geometric phase effect was incorporated into our calculations using gauge theory.[19–22] Further details of our calculations can be found in Ref. 11.

Calculated energies of the vibrational eigenstates are given in Table I, where the states are grouped into several pseudorotational progressions. Different progressions correspond to different values of the breathing (symmetric stretching) and bending quantum numbers v_1 and v_2, respectively. Within each progression, the states are labeled by the pseudorotational angular momentum quantum number m, which takes half-integer values (due to the geometric phase effect) and by the state symmetry: E, A_1, and A_2. There is always a pair of states with the same value of m, one is symmetric (m^+) and another is antisymmetric (m^-). However, the states of E-symmetry are doubly degenerate so that only one energy value is given in Table I, while the states of A-symmetry are split (A_1 and A_2) and both energy values are given. The largest value of the A_1-A_2 splitting corresponds to the lowest energy pair of nondegenerate states. For example, in the $(v_1=0,\ v_2=0,\ m)$ progression, the A_1-A_2 splitting is $\delta=100.46\ \mathrm{cm}^{-1}$ for $m=3/2$ states, it drops down to δ

TABLE I. Energies of vibrational states of cyclic-N_3 arranged into pseudorotational progressions (v_1,v_2,m).

v_1,v_2	$\lvert m\rvert$	Symmetry	Energy (cm^{-1})
(0, 0)	1/2	E	1325.67
	3/2	A_1	1401.22
		A_2	1501.68
	5/2	E	1668.88
	7/2	E	1944.56
	9/2	A_1	2269.93[a]
		A_2	2272.38
	11/2	E	2634.44
	13/2	E	2981.24
	15/2	A_1	3435.95
		A_2	3436.32
	17/2	E	3861.90
	19/2	E	4297.47
(0, 1)	1/2	E	2151.49
	3/2	A_1	2262.31[a]
		A_2	2339.15
	5/2	E	2540.71
	7/2	E	2828.28
	9/2	A_1	3175.60
		A_2	3183.82
	11/2	E	3546.25
	13/2	E	3939.78
	15/2	A_1	4349.79
		A_2	4350.35
(1, 0)	1/2	E	2888.24
	3/2	A_1	3003.67
		A_2	3038.19
	5/2	E	3257.48
	7/2	E	3557.27
	9/2	A_1	3928.34
		A_2	3937.11
	11/2	E	4309.19
(0, 2)	1/2	E	3025.22
	3/2	A_1	3123.31
		A_2	3176.02
	5/2	E	3409.79
	7/2	E	3735.22
	9/2	A_1	4071.50
		A_2	4078.60
	11/2	E	4449.09
(1, 1)	1/2	E	3690.31
	3/2	A_1	3871.90
		A_2	3869.42
	5/2	E	4148.60
(0, 3)	1/2	E	3816.54
	3/2	A_1	3984.73
		A_2	4017.89
	5/2	E	4276.10
(2, 0)	1/2	E	4419.59
	3/2	A_1	4601.27
		A_2	4576.80

[a]These two states exhibit strong coupling of bending to pseudorotation. Assigned quantum numbers are not good quantum numbers.

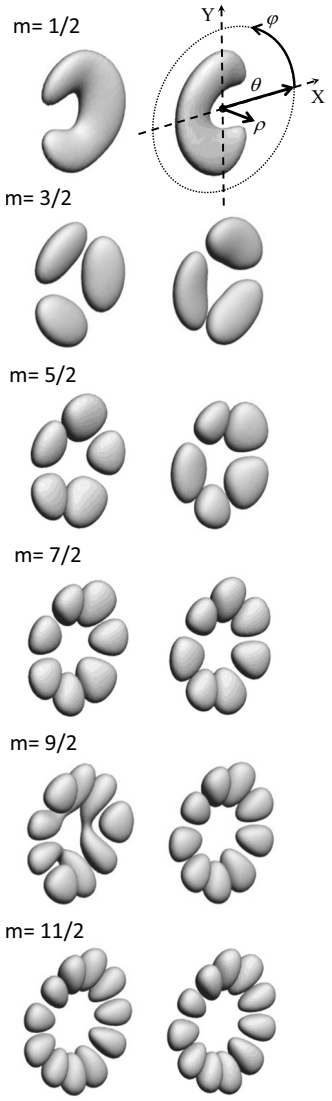

FIG. 1. 3D wave functions $\psi_i(\rho,\theta,\varphi)$ of the $(0,0,m)$ pseudorotational progression in cyclic-N_3. Functions up to $m=11/2$ are presented. For E-symmetry states two degenerate wave functions are shown. For the nondegenerate states the wave functions of symmetries A_1 and A_2 are shown. Explanation of the APH coordinates (ρ,θ,φ) and of the projection coordinates (X,Y) are given at the top.

$=2.45\ \text{cm}^{-1}$ for $m=9/2$ states, and is only $\delta=0.37\ \text{cm}^{-1}$ for $m=15/2$ states. Normally, the states of symmetry A_1 show lower energy than their counterparts of symmetry A_2. This order is violated only at the very high energies when the vibrational motion is excited. Examples are found in the following two pairs of A-symmetry states: $(v_1,v_2,m)=(1,1,3/2)$ and $(v_1,v_2,m)=(2,0,3/2)$. We attribute this effect to the coupling between the pseudorotational and vibrational modes due to the potential energy surface.

Vibrational wave functions $\psi_i(\rho,\theta,\varphi)$ for several states of the $(0,0,m)$-progression are presented in Fig. 1 using the hyperspherical projection coordinates X and Y defined as

$$X=\cos(\varphi)\cdot\tan(\theta/2), \tag{1}$$

$$Y=\sin(\varphi)\cdot\tan(\theta/2). \tag{2}$$

Each of wave functions in Fig. 1 encircles conical intersection, which is located at origin $(X,Y)=(0,0)$. The motion around the conical intersection corresponds to pseudorotation and is described by the hyperangle φ. In each frame of Fig. 1 this coordinate is simply the polar angle covering the range of $-\pi<\varphi<\pi$. As pseudorotational excitation increases, the wave functions develop more and more nodes along the hyperangle φ. On a qualitative level, the nodal structure of these wave functions along φ can be described by

$$\psi^{+}=\frac{1}{\sqrt{\pi}}\cos(m\varphi) \tag{3}$$

and

$$\psi^{-}=\frac{i}{\sqrt{\pi}}\sin(m\varphi) \tag{4}$$

dependencies for symmetric (m^{+}, left column of Fig. 1) and antisymmetric (m^{-}, right column of Fig. 1) states, respectively, where m is the pseudorotational angular momentum quantum number. Effect of the geometric phase is apparent in these vibrational wave functions. Namely, for any half-integer m, the ψ^{-} function is double valued at $\varphi=\pm\pi$

$$\psi^{-}(-\pi)=-\psi^{-}(+\pi) \tag{5}$$

i.e., it changes sign when the vibrational motion encircled the conical intersection. In a similar manner, the ψ^{+} functions change the sign of derivative at $\varphi=\pm\pi$. For any half-integer m we obtain

$$\frac{\partial}{\partial\varphi}\psi^{+}(-\pi)=-\frac{\partial}{\partial\varphi}\psi^{+}(+\pi). \tag{6}$$

As explained elsewhere,[11] these properties of the vibrational wave functions allow canceling the sign change of the electronic wave function, which occurs in Jahn–Teller molecules when the conical intersection is encircled.

Note that all wave functions of the $(0,0,m)$-progression shown in Fig. 1 correspond to purely pseudorotational excitation, and no vibrational excitation. It helps to keep in mind that the breathing motion (v_1) is described by the hyperradial coordinate ρ, which is plotted in Fig. 1 in the direction perpendicular to the plane of the pseudorotational motion, while the bending motion (v_2) is described by the hyperangle θ, which is plotted in Fig. 1 along the radial direction. Excitation of these modes leads to appearance of nodes along ρ and θ. All wave functions of cyclic-N_3 can be found in Ref. 11.

B. Dipole moment vector function

The dipole moment function of cyclic-N_3 was computed in this work at the same level of the electronic structure theory that was used to calculate the potential energy surface in our previous work.[10] The accurate description of N–N bonds requires a large atomic basis set. We employed the Dunning's standard correlation-consistent polarized valence triple-zeta basis set augmented with diffuse functions (aug-cc-pVTZ). To describe the multiconfiguration nature of the cyclic-N_3 radical, we employed the internally contracted multireference configuration interaction method with all singles and doubles (MRCISD) wave functions.[23] To all

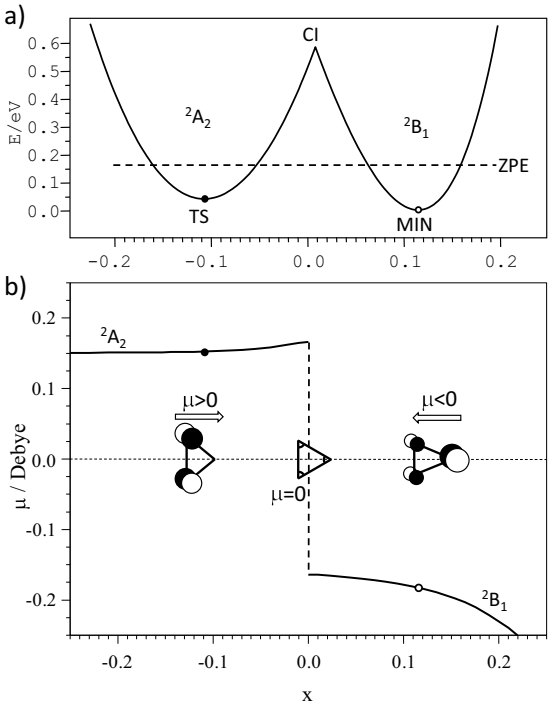

FIG. 2. One-dimensional slice along the $Y=0$ line through (a) the potential energy surface and (b) the dipole moment function of cyclic-N_3. The points of minimum (open circle), conical intersection ($X=0$), and the pseudorotational barrier (filed circle) are clearly seen. Symmetry of the electronic state wave function changes from $^2B_1$ to $^2A_2$ as we pass through the conical intersection. Direction of the dipole moment vector also changes. The zero-point energy of cyclic-N_3 and the structure of its HOMOs in the two states are shown.

MRCISD energies we applied the multireference version of the Davidson correction[24] that can be denoted as MRCISD(Q). In the MRCISD(Q) calculations, the reference wave function was obtained from the corresponding full valence CASSCF calculations consisting of 15 electrons distributed in 12 molecular orbitals, and only the 1*s* orbitals of N atoms were kept doubly occupied in all configurations while the remaining 15 electrons were correlated, denoted as MRCISD(Q) (15e/12o) aug-cc-pVTZ. The MOLPRO 2002.6 program was used to perform these calculations.[25]

One-dimensional slices are shown in Fig. 2 of the potential energy surface [Fig. 2(a)] and of the dipole moment function [Fig. 2(b)]. These slices go along the C_{2v} symmetry line ($Y=0$) through the following important points:

(1) The transition state point, which represents only a tiny barrier to pseudorotation due to large zero-point energy. In the vicinity of this point cyclic-N_3 has a shape of an *obtuse* isosceles triangle, and the symmetry of the adiabatic ground electronic state wave function is $^2A_2$. The dipole moment vector for such geometries points toward the apex of the cyclic-N_3 triangle (i.e., it is positive, $\boldsymbol{\mu}>0$). This is understood from analysis of the structure of highest occupied molecular orbital (HOMO) orbital for the $^2A_2$ state, which is located on the two terminal nitrogen atoms [see Fig. 2(b), left part].

(2) The minimum energy point which, due to an almost free pseudorotation, does not really represents a point of localization of the vibrational wave functions. In the vicinity of minimum the cyclic-N_3 has a shape of an *acute* isosceles triangle, and the symmetry of the adiabatic electronic ground state wave function is $^2B_1$. The dipole moment vector for such geometries points toward the base of the cyclic-N_3 triangle (i.e., it is negative, $\boldsymbol{\mu}<0$). This is again explained by the structure of HOMO orbital for the $^2B_1$ state, which is localized mostly on the apex nitrogen atom [see Fig. 2(b), right part].

(3) The conical intersection point, where cyclic-N_3 has shape of an equilateral triangle, while the two states of the electronic doublet, $^2A_2$ and $^2B_1$, are degenerate. We found that values of the dipole moments of two electronic states become equal at the point of conical intersection and, since they point in the opposite directions, cancel each other completely, resulting in zero dipole moment for the equilateral triangle configurations of cyclic-N_3. Note that zero dipole moment for the equilateral triangle configuration of a triatomic molecule could be predicted (expected) based on very general arguments.

Properties described above lead to a discontinuity (sign change) of the dipole moment for the adiabatic ground electronic state of cyclic-N_3, when its geometry is distorted along the C_{2v} symmetry line from the acute isosceles, through the equilateral to the obtuse isosceles triangle configuration (minimum → conical intersection → transition state), which is illustrated in Fig. 2(b). This feature, however, does not represent any problem or difficulty, simply because the vibrational wave functions of cyclic-N_3 never approach the point of conical intersection; they go around it. Indeed, as it can be seen from Fig. 1, all the $m>0$ wave functions vanish at the origin due to symmetry, while the $m=0$ vibrational state is forbidden due to the geometric phase effect.[26–32] Behavior of the dipole moment function as we go around the conical intersection is discussed next.

Using APH coordinates we set up a dense rectangular grid in three dimensions: 19 points in ρ covering the range from 3.18 to 3.93 a.u., 20 points in θ covering the range from zero to $X=\tan(\theta/2)=0.29$; and seven points covering the range of φ from zero to 60°. Electronic structure calculations were performed for all geometries on this grid, which resulted in the 2546 points determined *ab initio*. Between the *ab initio* points, accurate three-dimensional interpolants have been constructed using the tensor product *B*-cubic spline representation,[33] separately for $\mu_Q(\rho,\theta,\varphi)$ and $\mu_q(\rho,\theta,\varphi)$ functions-two components of the dipole moment vector.

Two components of the dipole moment vector, μ_Q and μ_q, as calculated by MOLPRO package, are projections of the dipole moment vector $\boldsymbol{\mu}$ onto the instantaneous principal axes of inertia of the molecule, **Q** and **q**. As in Ref. 34, we associate *Q*-axis with the smaller principal moment of inertia, and *q*-axis with the larger moment. According to this convention, in the acute isosceles triangle configurations, **Q** points along the symmetry line, while in the obtuse isosceles triangle configurations, **q** points along the symmetry line (see Fig. 3). It is important to realize that the pseudorotational

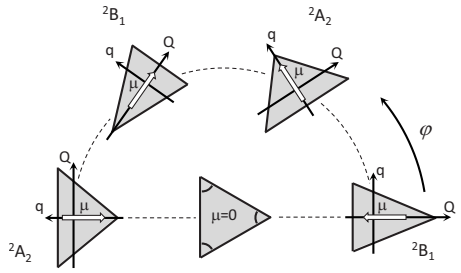

FIG. 3. Explanation of rotation of the dipole moment vector $\boldsymbol{\mu}$ in the body-fixed reference frame $(\mathbf{Q},\mathbf{q})$, and of rotation of the body-fixed frame in space, as the pseudorotational coordinate (the hyperangle φ) is increased from zero to π. As φ is changed, the shape of cyclic-N_3 is distorted as shown in the picture. Four geometries shown belong to C_{2v} symmetry and correspond to the equivalent energy minima on the PES ($\varphi=0$ and $2\pi/3$) and to the pseudorotational barriers on the PES ($\varphi=\pi/3$ and π). The vector $\boldsymbol{\mu}$ rotates clockwise, while the $(\mathbf{Q},\mathbf{q})$-frame rotates counterclockwise. Fifth geometry (D_{3h}) shown at origin corresponds to conical intersection.

motion along φ leads to rotation of the dipole moment vector $\boldsymbol{\mu}$ with respect to the $(\mathbf{Q},\mathbf{q})$ reference frame, as demonstrated in Fig. 3. At $\varphi=0$ (C_{2v}, acute isosceles) vector $\boldsymbol{\mu}$ is antiparallel with $\mathbf{Q}$ and we have nonzero negative μ_Q, such that $\mu_Q=-|\boldsymbol{\mu}|$, and $\mu_q=0$. When φ increases, the shape of the triangle distorts into C_s symmetry while the dipole moment vector rotates clockwise, leading to the monotonic conversion of μ_Q into μ_q. When φ reaches the value of $\pi/3$ (C_{2v}, obtuse isosceles) vector $\boldsymbol{\mu}$ becomes parallel to $\mathbf{q}$ and we have $\mu_Q=0$, $\mu_q=|\boldsymbol{\mu}|$. This transformation proceeds further to $\varphi=2\pi/3$ (acute isosceles) and to $\varphi=\pi$ (obtuse isosceles) as shown in Fig. 3. Overall, when φ is varied from zero to π, the dipole moment vector $\boldsymbol{\mu}$ rotates clockwise by $3\pi/2$ relative to the $(\mathbf{Q},\mathbf{q})$ reference frame. Note that the actual *ab initio* calculations are performed only in the range of $0<\varphi<\pi/3$, and the data are reflected several times to cover the entire $-\pi<\varphi<+\pi$ range.

It is also important to realize that the pseudorotational motion along φ rotates in space the $(\mathbf{Q},\mathbf{q})$-frame itself, as demonstrated in Fig. 3. This rotation was described in the original paper by Parker and Pack[34] where the APH coordinates were introduced. They showed that the rotation that transforms the mass-scaled Jacoby vector $\mathbf{S}$ into the vector $\mathbf{Q}$ is given by

$$\sin\beta=\frac{s\sin\Theta\sin\frac{\varphi}{2}}{\left[\left(s\sin\Theta\sin\frac{\varphi}{2}\right)^2+\left(S\cos\frac{\varphi}{2}+s\cos\Theta\sin\frac{\varphi}{2}\right)^2\right]^{1/2}},\tag{7}$$

$$\cos\beta=\frac{S\cos\frac{\varphi}{2}+s\cos\Theta\sin\frac{\varphi}{2}}{\left[\left(s\sin\Theta\sin\frac{\varphi}{2}\right)^2+\left(S\cos\frac{\varphi}{2}+s\cos\Theta\sin\frac{\varphi}{2}\right)^2\right]^{1/2}},\tag{8}$$

where S, s, and Θ are usual mass scale Jacoby coordinates of one of the arrangement channels. (Note that our hyperangle φ is related to the hyperangle χ of Parker and Pack as $\varphi=2\chi$.) The value of β changes smoothly from zero to $\pi/2$ as φ is varied from zero to π (see Fig. 3). Since the $(\mathbf{Q},\mathbf{q})$-frame rotates counterclockwise, the dipole moment vector $\boldsymbol{\mu}$ rotates in the laboratory frame by π (clockwise, see Fig. 3) as φ is varied from zero to π.

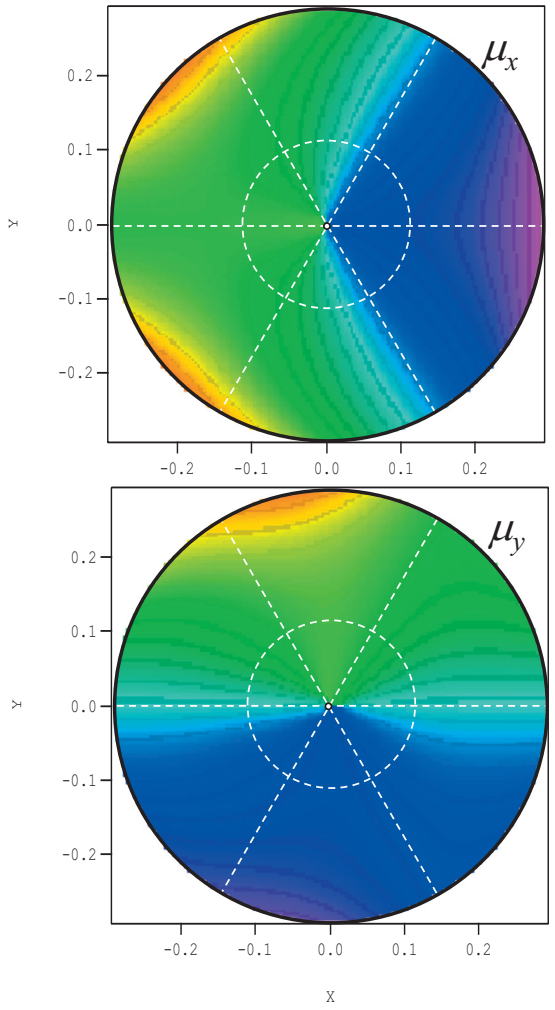

FIG. 4. Two-dimensional slices through the components $\mu_x(\rho,\theta,\varphi)$ and $\mu_y(\rho,\theta,\varphi)$ of the dipole moment vector function of cyclic-N_3 in the space-frame. Violet color indicated negative and red color indicated positive sign of the vector; the range is from -0.34 to $+0.34$ D (with light blue color corresponding to zero dipole moment). Location of conical intersection is shown by a dot. The minimum energy path for pseudorotation is indicated approximately by white dashed circle. White lines show the C_{2v} symmetry lines in the hyperspherical projection configuration space.

Note that the one-dimensional slice of Fig. 3 along the C_{2v} symmetry line ($Y=0$) shows sign change of the dipole moment vector in the D_{3h} configuration (equilateral triangle), as we pass the conical intersection, consistent with Fig. 2(b).

If we choose to "embed" the Jacoby vector $\mathbf{S}$ into the laboratory frame, the two space frame components of the dipole moment vector function are obtained as

$$\mu_x(\rho,\theta,\varphi)=\mu_Q(\rho,\theta,\varphi)\cdot\cos\beta-\mu_q(\rho,\theta,\varphi)\cdot\sin\beta,\tag{9}$$

$$\mu_y(\rho,\theta,\varphi)=\mu_Q(\rho,\theta,\varphi)\cdot\sin\beta+\mu_q(\rho,\theta,\varphi)\cdot\cos\beta.\tag{10}$$

Here, as in Ref. 16, we chose the laboratory frame axis z to be perpendicular to the plane of the triatomic, so that μ_z is zero due to symmetry. Figure 4 shows two-dimensional

slices of $\mu_x(\rho,\theta,\varphi)$ and $\mu_y(\rho,\theta,\varphi)$ calculated using Eqs. (7)–(10). In these pictures the value of hyper-radius ρ is fixed at the minimum energy point $\rho_{eq}=3.4656$ Bohr, while the values of θ and φ are varied. We see that both components of the dipole moment vector $\boldsymbol{\mu}$ change smoothly through the entire configuration space. The function $\mu_x(\rho,\theta,\varphi)$ is symmetric, while the function $\mu_y(\rho,\theta,\varphi)$ is antisymmetric with respect to reflection through the C_{2v} symmetry line ($Y=0$). Further analysis shows that on average the change of the dipole moment is relatively weak along both θ (bending) and ρ (breathing) coordinates, but it is much more significant along the pseudorotational coordinate φ. Thus, one should expect higher intensities of transitions between states of the pseudorotational progression, and weaker intensities of transitions between different progressions.

C. Construction of the infrared (IR) absorption spectrum

The matrix elements

$$\mu_{ij}^{(x)}=\langle\psi_j(\rho,\theta,\varphi)|\mu_x(\rho,\theta,\varphi)|\psi_i(\rho,\theta,\varphi)\rangle, \tag{11}$$

$$\mu_{ij}^{(y)}=\langle\psi_j(\rho,\theta,\varphi)|\mu_y(\rho,\theta,\varphi)|\psi_i(\rho,\theta,\varphi)\rangle \tag{12}$$

were integrated in the hyperspherical coordinates and used to calculate the permanent dipole moment and the line strengths

$$S_v=\sum_i\sum_j(|\mu_{ij}^{(x)}|^2+|\mu_{ij}^{(y)}|^2). \tag{13}$$

The integrated absorption coefficients were computed as[35]

$$I_v=\frac{8\pi^3N_A\nu}{4\pi\varepsilon_0 3hc}\frac{\exp(-E_i/kT)[1-\exp(-hc\nu/kT)]}{g}S_v. \tag{14}$$

Summation in Eq. (13) is over all degenerate vibrational initial and final states contributing to the transition at the wave number ν; $g=\Sigma\exp(-E_k/kT)$ is the partition function, where sum is over all states of the molecule. Note that the nuclear spin statistics and the angular momentum weights are not implemented here. Rigorous incorporation of these factors requires calculations with $J>0$, which goes beyond the scope of this paper and will be reported elsewhere.[36]

Cyclic-N_3 molecules produced in the recent molecular beam experiments are rotationally cold,[1,2,4–7] but their vibrational temperature appears to be high, about 300 K, due to no vibrational relaxation following the photodissociation of ClN_3. At this temperature, several low lying pseudorotational states of cyclic-N_3 are populated and may serve as the initial states for the IR transitions. For example, the first exited state is only about 75 cm^{-1} above the ground pseudorotational state. In this work we consider five lower pseudorotational states as thermally populated initial states. These are (see Table I) three lowest doubly degenerate states of E-symmetry: $m=1/2$, 5/2, and 7/2, and the lowest pair of nondegenerate states with $m=3/2$ (symmetries are A_1 and A_2). All these states belong to the vibrationless pseudorotational progression $(0,0,m)$. Wave functions of these states are included in Fig. 1. Populations of all upper states (above 2000 cm^{-1}) are insignificant, less than 1% of the ground vibrational state population at 300 K. These upper states were not included in our calculations as the initial states. All the states included in Table I were considered as final states in our calculations of the dipole moment matrix elements and construction of the spectra, Eqs. (11)–(14).

TABLE II. Most important dipole moment matrix elements in cyclic-N_3.

States and symmetries	$\mu_{ij}^{(x)}$/mD	$\mu_{ij}^{(y)}$/mD
Permanent dipole moments:		
$m^{\pm}=1/2$	96.332	82.450
	77.306	82.450
$m^{+}=3/2$	9.314	···
$m^{-}=3/2$	10.024	···
$m^{\pm}=5/2$	0.850	7.562
	20.800	7.562
$m^{\pm}=7/2$	17.625	6.967
	3.307	6.967
Transition dipole moments:		
$m^{\pm}=1/2\rightarrow m^{+}=3/2$	107.987	96.000
$m^{\pm}=1/2\rightarrow m^{-}=3/2$	58.526	65.727
$m^{+}=3/2\rightarrow m^{\pm}=5/2$	66.268	66.395
$m^{-}=3/2\rightarrow m^{\pm}=5/2$	95.797	93.920
$m^{\pm}=5/2\rightarrow m^{\pm}=7/2$	81.797	80.315
	82.152	80.648
$m^{\pm}=7/2\rightarrow m^{+}=9/2$	76.713	72.970
$m^{\pm}=7/2\rightarrow m^{-}=9/2$	81.203	79.864
$m^{\pm}=7/2\rightarrow m^{+}=3/2,\ v_2=1$	35.002	32.698

III. RESULTS AND DISCUSSION

In Table II we collected the most important off-diagonal (transition) dipole moment matrix elements $\mu_{ij}^{(x)}$ and $\mu_{ij}^{(y)}$ and all diagonal (permanent) dipole moment matrix elements $\mu_{ii}^{(x)}$ and $\mu_{ii}^{(y)}$ Since the E-symmetry states are doubly degenerate, eight possible matrix elements can be formed between two E-symmetry states using two components of the dipole moment vector function. Among them, four are exactly zero due to symmetry

$$\langle E^+|\mu_y|E^+\rangle=0,\quad \langle E^-|\mu_y|E^-\rangle=0,$$
$$\langle E^-|\mu_x|E^+\rangle=0,\quad \langle E^+|\mu_x|E^-\rangle=0 \tag{15}$$

and four are nonzero elements

$$\langle E^+|\mu_x|E^+\rangle\neq 0,\quad \langle E^-|\mu_x|E^-\rangle\neq 0,$$
$$\langle E^-|\mu_y|E^+\rangle\neq 0,\quad \langle E^+|\mu_y|E^-\rangle\neq 0. \tag{16}$$

Similarly, four matrix elements can be formed between an A-symmetry state and an E-symmetry state. For symmetry A_1

$$\langle E^+|\mu_y|A_1\rangle=0,\quad \langle E^-|\mu_x|A_1\rangle=0 \tag{17}$$

and

$$\langle E^+|\mu_x|A_1\rangle\neq 0,\quad \langle E^-|\mu_y|A_1\rangle\neq 0. \tag{18}$$

For symmetry A_2

$$\langle E^-|\mu_y|A_2\rangle=0,\quad \langle E^+|\mu_x|A_2\rangle=0 \tag{19}$$

and

$$\langle E^-|\mu_x|A_2\rangle \neq 0, \quad \langle E^+|\mu_y|A_2\rangle \neq 0. \tag{20}$$

For elements between two states of A-symmetry

$$\langle A_1|\mu_y|A_1\rangle = 0, \quad \langle A_2|\mu_y|A_2\rangle = 0, \quad \langle A_2|\mu_x|A_1\rangle = 0 \tag{21}$$

and

$$\langle A_1|\mu_x|A_1\rangle \neq 0, \quad \langle A_2|\mu_x|A_2\rangle \neq 0, \quad \langle A_2|\mu_y|A_1\rangle \neq 0. \tag{22}$$

Matrix elements that are exactly zero due to symmetry were not included into Table II.

A. Permanent dipole moment

Analysis of the diagonal matrix elements in Table II shows that the ground vibrational state of cyclic-N_3, $(v_1,v_2,m)=(0,0,1/2)$, exhibits the most significant permanent dipole moment. Four nonzero matrix elements for this state range from 77.3 to 96.3 mD. Note that the value of the dipole moment at the point of minimum on the potential energy surface is about 180 mD, while at the point of pseudorotational barrier it is about 160 mD (see Fig. 2). Thus, averaging over the vibrational wave function reduces the value of dipole moment roughly by a factor of 2. This observation is consistent with a simple model for pseudorotational motion in cyclic-N_3 that will be published elsewhere.[36]

Upper states of cyclic-N_3 studied in this work show a significantly smaller dipole moment matrix elements, only about 10.0 mD for $m=3/2$ states of A-symmetry, and only about 20.0 mD for $m=5/2$ and 7/2 states of E-symmetry. This allows us to conclude that the dipole moment of cyclic-N_3 decreases as temperature increases, due to thermal population shifting toward the excited pseudorotational states with much lower permanent dipole moment.

Note that the four matrix elements given in Table II for each doubly degenerate state of E-symmetry can be used to set up a 2×2 dipole moment matrix for each doubly degenerate state: $\langle m^+|\mu|m^+\rangle$, $\langle m^+|\mu|m^-\rangle=\langle m^-|\mu|m^+\rangle$, and $\langle m^-|\mu|m^-\rangle$. Diagonalization of this matrix is also equivalent to the treatment of Stark effect within the first order of perturbation theory. This procedure gives following values for the three lowest vibrational states of E-symmetry studied here:

$$\mu_{1/2^+} = 169.816 \text{ mD}, \quad \mu_{1/2^-} = 3.822 \text{ mD},$$

$$\mu_{5/2^+} = 23.342 \text{ mD}, \quad \mu_{5/2^-} = 1.692 \text{ mD},$$

$$\mu_{7/2^+} = 20.456 \text{ mD}, \quad \mu_{7/2^-} = 0.476 \text{ mD}.$$

We see that the dipole moments of two components of doubly degenerate states of E-symmetry are different, which should lead to splitting of the degenerate states in the external electric field. This information can be useful in the experimental studies of Stark effect in cyclic-N_3.

B. Transition dipole moment

The most important elements of the transition moment matrix in cyclic-N_3 correspond to excitation of the pseudorotational progression of states, when the transition is described by the following changes of quantum numbers:

$$\Delta v_1 = 0, \quad \Delta v_2 = 0, \quad \Delta m = +1. \tag{23}$$

The values of matrix elements for these transitions vary in the range between 58.5 and 108.0 mD. Other groups of transitions exhibit much smaller transition moments. For comparison, we found that among the transitions with smaller transition moments, there are two groups of transitions characterized by the following changes of quantum numbers:

$$\Delta v_1 = 0, \quad \Delta v_2 = +1, \quad \Delta m = +1 \tag{24}$$

and

$$\Delta v_1 = +1, \quad \Delta v_2 = 0, \quad \Delta m = -1. \tag{25}$$

The most important of these transitions exhibit transition moments in the rage of 0.1 mD. Other two groups of transitions

$$\Delta v_1 = 0, \quad \Delta v_2 = 0, \quad \Delta m = +2 \tag{26}$$

and

$$\Delta v_1 = 0, \quad \Delta v_2 = +1, \quad \Delta m = -1 \tag{27}$$

exhibit transition moments in the rage of 0.05 mD. Finally, the group of transitions with

$$\Delta v_1 = +1, \quad \Delta v_2 = 0, \quad \Delta m = +2 \tag{28}$$

exhibit transition moments in the rage of 0.01 mD.

There is one more strange transition that exhibits a relatively large value of the transition dipole moment

$$(0,0,7/2) \rightarrow (0,1,3/2). \tag{29}$$

The nonzero matrix elements for this transition are 35.0 and 32.7 mD. This transition does not belong to any group of transitions discussed above and stands by itself. Note, however, that energy of the (0, 1, 3/2) state at 2262.31 cm^{-1} is very close to energy of the purely pseudorotational state (0, 0, 9/2), which is at 2269.93 cm^{-1}. Both states belong to symmetry A_1 and, being separated by less than 8 cm^{-1}, show very strong interaction. Their wave functions show mixed character. Namely, the wave function of state at 2269.93 cm^{-1}, although labeled here as (0, 0, 9/2) for convenience, shows a significant degree of the bending excitation toward $v_2=1$ (seen very clearly in Fig. 1). In an analogous manner, the wave function of state at 2262.31 cm^{-1}, although labeled here as (0, 1, 3/2) for convenience, shows a significant degree of the pseudorotational excitation toward $m=9/2$ (not shown here, see Fig. 7 in Ref. 11). Thus, similarity of the wave-function of the (0, 1, 3/2) state to the purely pseudorotational wave function (0, 0, 9/2) leads to increased overlaps and large transition moments of this standalone transition in Eq. (29).

C. IR absorption spectrum

The most intense part of the predicted IR absorption spectrum is shown in Fig. 5. It includes seven purely pseudorotational excitation transitions with $\Delta m=+1$, Eq. (23). First five of these transitions dominate the spectrum, with the values of absolute integrated absorption coefficients in the

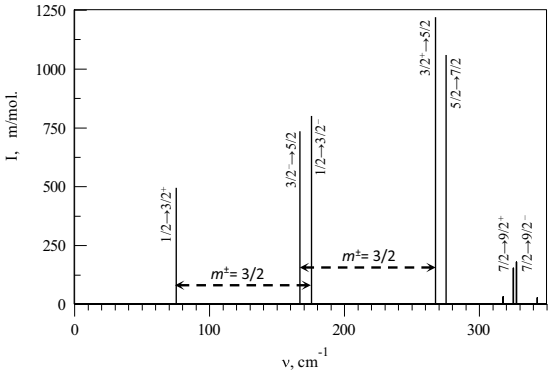

FIG. 5. Far IR intense part of the absorption spectrum of cyclic-N_3. Transitions correspond to excitation of the pseudorotational progression. The splittings of nondegenerate states of symmetries A_1-A_2 manifest themselves in the spectrum, as shown by arrows.

range between 0.5 and 1.2 km/mol. Frequencies of these five transitions are in the 75–275 cm^{-1} region, which is far IR. The transition of Eq. (29) is also in this part of spectrum but it is much weaker. We predict that the most intense is an $m=3/2(A_1)\rightarrow m=5/2(E)$ transition at 267.66 cm^{-1} (see Fig. 5).

The A_1-A_2 splitting of the $m=3/2$ state manifests twice in this part of spectrum, as shown in Fig. 5. Note that this effect does not look like a splitting at all, simply because the value of splitting, $\delta=100.46$ cm^{-1}, is greater than frequency of transition, which is only 75.55 cm^{-1}. This feature is quite unusual and can serve as a spectroscopic probe of cyclic-N_3. The A_1-A_2 splitting of the $m=9/2$ state, $\delta=2.45$ cm^{-1}, is relatively small and is seen as an actual splitting at roughly 325 cm^{-1}.

The weak part of the absorption spectrum is shown in Fig. 6 in the wide range from 350 to 3500 cm^{-1}. Many of these transitions involve excitation of the bending and/or breathing modes v_2 and v_1, their combinations and overtones, but some transitions are due to excitations of two pseudorotational quanta simultaneously, $\Delta m=+2$. Four groups of transitions are identified:

- First band in the 350–750 cm^{-1} range corresponds to transitions given by Eqs. (26) and (27).

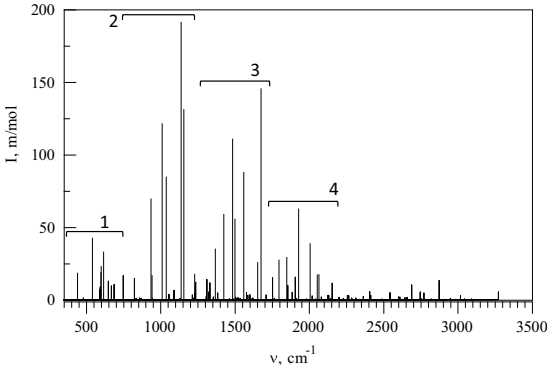

FIG. 6. Weak part of the absorption spectrum of cyclic-N_3. Three bands are identified. They correspond to excitation of bending and breathing modes, their overtones, and combinations, as well as excitation of two pseudorotational quanta simultaneously. See text for details.

- Second band in the 750–1250 cm^{-1} range contains transitions given by Eq. (24).
- Third band in the 1250–1750 cm^{-1} range contains transitions given by Eq. (25), but also some $\Delta v_1=+1$, $\Delta v_2=0$ transitions with $\Delta m=0,+1$, and some $\Delta v_1=0$, $\Delta v_2=+1$ transitions with $\Delta m=+2,+3$.
- Fourth band in the 1750–2250 cm^{-1} range contains transitions given by Eq. (28) but also $\Delta v_1=0$, $\Delta v_2=+2$, $\Delta m=+1$ transitions.

As readers can see from Fig. 6, this part of spectrum contains many spectral lines. It can, however, be analyzed in greater detail if it is needed for the experimental purposes. For example, the A_1-A_2 splitting of both $m=3/2$ and $m=9/2$ states manifest in several places in these spectra and can be easily identified.

IV. CONCLUSIONS

We have carried out the first prediction of the IR absorption spectrum of cyclic-N_3. Accurate vibrational energies and wave functions were calculated with incorporation of the geometric phase effect (using gage theory) on accurate potential energy surface. A sophisticated fully dimensional dipole moment function was constructed using accurate *ab initio* calculations on three-dimensional-grid and spline interpolation. Transformation of the dipole moment vector function from the reference frame associated with the instantaneous principal axes of inertia to the laboratory-fixed reference frame was carried out using hyperspherical coordinates. All matrix elements were computed numerically.

The resultant permanent dipole moment of cyclic-N_3 in the ground vibrational state is relatively small (170 mD). The permanent dipole moments of the excited vibrational states are even smaller, on the order of only 10–25 mD.

The most intense part of the IR absorption spectrum is observed in the deep IR range, from 75 to 275 cm^{-1}. It includes only five transitions that correspond to excitation of the pseudorotational progression of states. The absolute values of absorption cross sections in this part of spectrum are in the range of 0.5–1.2 km/mol. Two large splittings (~100 cm^{-1}) and one small splitting (~2.5 cm^{-1}) are observed in this part of spectrum due to transitions involving nondegenerate states of symmetries A_1 and A_2. These features can be used as spectroscopic signatures of cyclic-N_3.

A significant number of weaker transitions is observed in the 350–3500 cm^{-1} part of spectrum. These transitions are due to vibrational (bending and breathing) excitations, various overtones, and the combination bands. The absolute values of absorption cross sections for the most intense of these transitions are only on the order of 0.1–0.2 km/mol. Although weaker, these transitions may also be very much usable for spectroscopy because this part of spectrum is easier to access experimentally.

From the results presented above it seems logical to search for cyclic-N_3 in the deep IR range. The fundamental transition, as predicted here, is at 75.55 cm^{-1}. Several unique splittings of very different magnitudes should help to identify cyclic-N_3.

ACKNOWLEDGMENTS

This work was supported by the Air Force Office of Scientific Research (Grant No. FA9550-09-1-0604). Scott Reid at Marquette University is acknowledged for many fruitful discussions. Peng Zhang and Keiji Morokuma at Emory University are acknowledged for their contribution to calculations of the dipole moment function. Part of this work was done under the auspices of the U.S. Department of Energy at Los Alamos National Laboratory. Los Alamos National Laboratory is operated by Los Alamos National Security, LLC, for the National Nuclear Security Administration of the U.S. Department of Energy under Contract No. DE-AC52-06NA25396. This research used resources of the National Energy Scientific Computing Center, which is supported by the Office of Science of the U.S. Department of Energy under Contract No. DE-AC02-05CH11231.

[1] N. Hansen and A. M. Wodtke, J. Phys. Chem. A **107**, 10608 (2003).
[2] N. Hansen, A. V. Komissarov, K. Morokuma, M. C. Heaven, and A. M. Wodtke, J. Chem. Phys. **118**, 10485 (2003).
[3] M. Bittererová, H. Ostmark, and T. Brink, J. Chem. Phys. **116**, 9740 (2002).
[4] A. M. Wodtke, N. Hansen, N. Sveum, J. Robinson, S. Goncher, and D. M. Neumark, Chem. Phys. Lett. **391**, 334 (2004).
[5] N. Hansen, A. M. Wodtke, S. J. Goncher, J. Robinson, N. Sveum, and D. M. Neumark, J. Chem. Phys. **123**, 104305 (2005).
[6] P. Samartzis, J. J.-M. Lee, T.-T. Ching, C. Chadhuri, Y. T. Lee, and A. M. Wodtke, J. Chem. Phys. **123**, 051101 (2005).
[7] P. Samartzis, J. J.-M. Lee, T.-T. Ching, C. Chadhuri, Y. T. Lee, and A. M. Wodtke, J. Chem. Phys. **126**, 041101 (2007).
[8] P. Samartzis and A. M. Wodtke, Int. Rev. Phys. Chem. **25**, 527 (2006).
[9] P. Samartzis and A. M. Wodtke, Phys. Chem. Chem. Phys. **9**, 3054 (2007).
[10] D. Babikov, P. Zhang, and K. Morokuma, J. Chem. Phys. **121**, 6743 (2004).
[11] D. Babikov, B. Kendrick, P. Zhang, and K. Morokuma, J. Chem. Phys. **122**, 044315 (2005).
[12] P. Zhang, K. Morokuma, and A. M. Wodtke, J. Chem. Phys. **122**, 014106 (2005).
[13] J. Zhang, Y. Chen, K. Yuan, S. A. Harich, X. Wang, X. Yang, P. Zhang, Z. Wang, K. Morokuma, and A. M. Wodtke, Phys. Chem. Chem. Phys. **8**, 1690 (2006).
[14] V. A. Mozhayskiy, D. Babikov, and A. I. Krylov, J. Chem. Phys. **124**, 224309 (2006).
[15] D. Babikov, V. A. Mozhayskiy, and A. I. Krylov, J. Chem. Phys. **125**, 084306 (2006).
[16] B. K. Kendrick, R. T. Pack, R. B. Walker, and E. F. Hayes, J. Chem. Phys. **110**, 6673 (1999) and references therein.
[17] B. K. Kendrick and R. T. Pack, J. Chem. Phys. **104**, 7475 (1996).
[18] B. R. Johnson, J. Chem. Phys. **67**, 4086 (1977); **68**, 4678 (1978).
[19] B. K. Kendrick, Phys. Rev. Lett. **79**, 2431 (1997).
[20] B. K. Kendrick, Int. J. Quantum Chem. **64**, 581 (1997).
[21] B. K. Kendrick and R. T. Pack, J. Chem. Phys. **106**, 3519 (1997).
[22] B. K. Kendrick, in *Conical Intersections: Electronic Structure, Dynamics, and Spectroscopy*, edited by W. Domcke, D. R. Yarkony, and H. Köppel (World Scientific, Singapore, 2004).
[23] H.-J. Werner and P. J. Knowles, J. Chem. Phys. **89**, 5803 (1988).
[24] D. R. Davidson, J. Comput. Phys. **17**, 87 (1975).
[25] MOLPRO, a package of *ab initio* programs designed by H.-J. Werner and P. J. Knowles, version 2002.1, R. D. Amos, A. Bernhardsson, A. Berning *et al.*.
[26] M. V. Berry, Proc. R. Soc. London, Ser. A **392**, 45 (1984).
[27] B. Lepetit and A. Kuppermann, Chem. Phys. Lett. **166**, 581 (1990).
[28] Y. S. M. Wu, A. Kuperman, and B. Lepetit, Chem. Phys. Lett. **186**, 319 (1991).
[29] C. A. Mead and D. G. Truhlar, J. Chem. Phys. **70**, 2284 (1979); C. A. Mead, *ibid.* **72**, 3839 (1980).
[30] C. A. Mead, Chem. Phys. **49**, 23 (1980).
[31] T. C. Thompson, D. G. Truhlar, and C. A. Mead, J. Chem. Phys. **82**, 2392 (1985).
[32] D. G. Truhlar, T. C. Thompson, and C. A. Mead, Chem. Phys. Lett. **127**, 287 (1986).
[33] C. de Boor, *A Practical Guide to Splines* (Springer, New York, 1978).
[34] R. T. Pack and G. A. Parker, J. Chem. Phys. **87**, 3888 (1987).
[35] *Molecular Symmetry and Spectroscopy*, 2nd ed., edited by P. R. Bunker and P. Jensen (NRC Research, Ottawa, 1998).
[36] D. Babikov and B. Kendrick, "Perturbation theory treatment of pseudo-rotation in cyclic-N_3," J. Chem. Phys. (to be submitted).